

Least-squares migration in the presence of velocity errors

Simon Luo & Dave Hale

Center for Wave Phenomena, Colorado School of Mines, Golden, CO 80401, USA

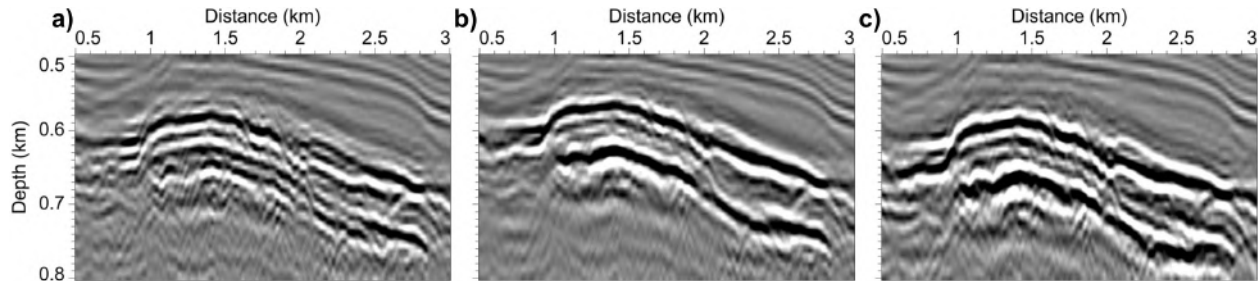


Figure 1. Least-squares migration images computed for a laterally invariant velocity model by minimizing the (a) difference between predicted and observed data, and (b) difference between predicted and *shifted* observed data. Compared to the (c) image computed for an optimized velocity model by minimizing the difference between predicted and observed data, the image in (b) contains similar features despite the use of a much simpler velocity model during migration.

ABSTRACT

Seismic migration requires an accurate background velocity model that correctly predicts the kinematics of wave propagation in the true subsurface. Least-squares migration, which seeks the inverse rather than the adjoint of a forward modeling operator, is especially sensitive to errors in this background model, which can result in traveltime differences between predicted and observed data that lead to incoherent and defocused migration images. We propose an alternative misfit function for use in least-squares migration that measures amplitude differences between predicted and observed data, i.e., differences after correcting for nonzero traveltime shifts between predicted and observed data. We demonstrate on synthetic and field data that, when the background velocity model is incorrect, the use of this misfit function results in better focused migration images with greater amplitude fidelity. Results suggest that our method best enhances image focusing when differences between predicted and observed data can be explained by traveltime shifts.

1 INTRODUCTION

Seismic migration can be described as the adjoint of a linearized forward modeling operator applied to observed data (Claerbout, 1992). Migration produces a reflectivity image, an image of a perturbation to the background velocity model (Cohen and Bleistein, 1979), that approximates the true reflectivity insofar as the adjoint of the forward operator approximates the pseudoinverse. Typically, the adjoint is a poor approximation, and the accuracy of the computed reflectivity image can be significantly improved by using the pseudoinverse of the forward operator rather than the adjoint. The use of the pseudoinverse of the forward operator in migration is known as least-squares migration (Nemeth

et al., 1999; Østmo and Plessix, 2002; Plessix and Mulder, 2004; Köhl and Sacchi, 2003; Dai, 2012).

Least-squares migration requires the inverse of the Hessian matrix (the normal operator) of second derivatives of a misfit function with respect to model parameters. The Hessian, however, is prohibitively expensive to compute and store for most practical-sized problems. Approximations of the inverse Hessian (Gray, 1997; Chavent and Plessix, 1999; Shin et al., 2001; Rickett, 2003; Guitton, 2004; Plessix and Mulder, 2004; Valenciano, 2008; Symes, 2008) are more feasible, and are often used to improve the quality of final migration images or to precondition iterative least-squares migration. In this paper, we focus on iterative least-squares migration,

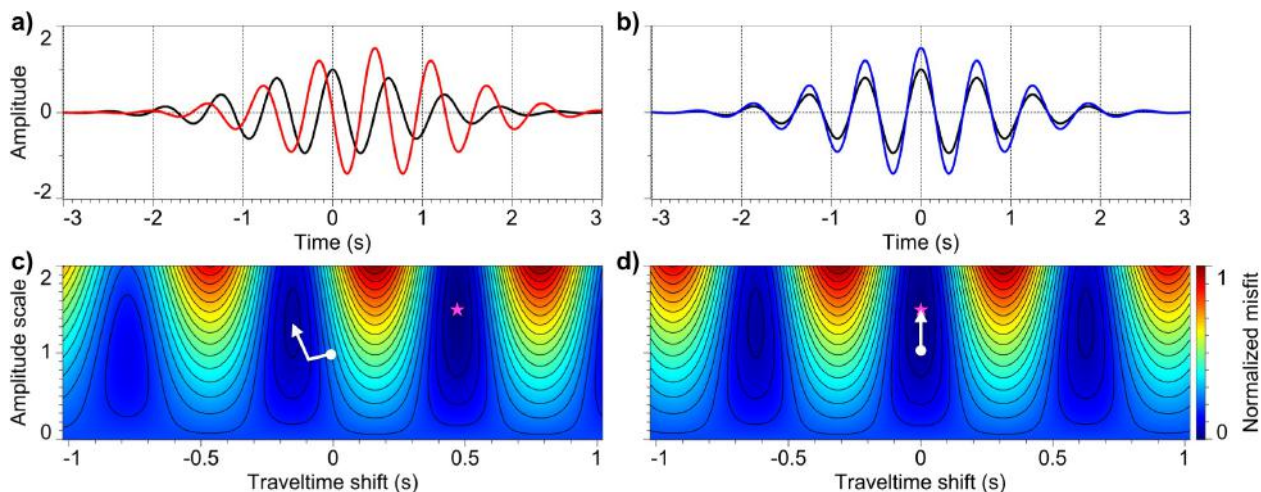


Figure 2. A simple example. The (a) predicted data (black) and observed data (red); (b) predicted data (black) and shifted observed data (blue); (c) normalized misfit function computed with the predicted and observed data shown in (a); and (d) normalized misfit function computed with the predicted and shifted observed data shown in (b). A local optimization method beginning at the position indicated by the white circle will converge to a local minimum in (c), but will find the global minimum, indicated by the magenta star, in (d).

which can be used in conjunction with or in place of approximations of the Hessian. An advantage of iterative migration algorithms is that they typically are straightforward to implement; a disadvantage is that they can be more computationally expensive compared to an efficient approximation of the Hessian, or compared to a single application of the adjoint operator as is done, for example, in reverse-time migration (Baysal et al., 1983; Loewenthal and Mufti, 1983; McMechan, 1983; Whitmore, 1983; Levin, 1984).

The quality and accuracy of migration images depends greatly on the accuracy of the background velocity model, and errors in this background model can lead to an incoherent, defocused image. Ideally, the background velocity model should correctly predict the traveltimes of observed data, and should be sufficiently smooth so as not to generate reflected waves. These requirements derive from the conditions under which the Born approximation is valid (Symes, 2009), and under these conditions, migration can accurately image subsurface structures. However, when these conditions are violated, migration images are degraded and become defocused and incoherent. One reason for this degradation is that migration inverts for the perturbation to the background velocity model that controls only the amplitudes of predicted data; if the background model contains errors, then the predicted data will contain errors in both traveltime and amplitude compared to the observed data, and both these types of errors — instead of only the amplitude errors — will contribute to the migration image.

Often, separating these types of errors, and perhaps discarding a certain type of error, can improve

inversion results. For example, for full waveform inversion (Tarantola, 1984; Pratt et al., 1998), authors advocate using only phase or traveltime information (Shin and Min, 2006; Bednar et al., 2007; Choi and Alkhalifah, 2011; Kamei et al., 2011), especially to update the low-wavenumber background model that is difficult for full waveform inversion to recover from reflection seismic data (Snieder et al., 1989; Hicks and Pratt, 2001; Xu, 2012; Ma, 2012). Our task in least-squares migration is complementary to that of full waveform inversion for the background model: we seek to invert for the high-wavenumber component of the model, i.e., the perturbation to the background model. Thus, analogous to the use of phase or traveltime information to recover the low-wavenumber component of the velocity model, we propose to use amplitude information to recover the high-wavenumber component.

The utility of this amplitude and traveltime separation is easily illustrated. Consider the task of estimating a traveltime shift and an amplitude scale between two 1D signals, shown in Figure 2. In Figures 2a and 2b, the black curve represents the predicted data, the red curve represents the observed data, and the blue curve represents the observed data shifted so that its traveltime matches that of the predicted data. The conventional least-squares misfit function, i.e., the L^2 -norm of the difference between predicted and (possibly shifted) observed data, for two model parameters (the amplitude scale and the traveltime shift) is shown in Figures 2c and 2d. Notice in Figures 2c and 2d the location of the global minimum, indicated by the magenta star. Figure 2c shows the normalized misfit function computed between predicted and observed data (Figure 2a). With

this misfit function, a local optimization method beginning at the location of the white circle will descend to a local minimum, indicated by the white arrow. In comparison, the normalized misfit function computed between predicted and *shifted* observed data (Figure 2b) shown in Figure 2d enables the global minimum to be found.

This simple example suggests that by first correcting for traveltime shifts between predicted and observed data, we are better able to estimate the component of the model that controls the amplitude (in this case, the amplitude scale). This is the approach we wish to pursue for the more complicated problem of least-squares migration. The simple example relied on the fact that we could correctly estimate the traveltime shift between predicted and observed data. For migration, we require an accurate and robust method for estimating traveltime shifts between two (not necessarily 1D) signals, and for this purpose we use dynamic warping (Hale, 2013).

We propose a simple modification of the conventional least-squares misfit function used in iterative least-squares migration. Rather than minimize the difference between predicted and observed data, we propose to minimize their difference after correcting for nonzero traveltime shifts. Assuming estimated traveltime shifts between predicted and observed data are accurate, this misfit function quantifies mostly amplitude differences. We demonstrate that the use of this amplitude misfit function in least-squares migration results in more coherent and better focused images when the background velocity model used for migration differs from the true background velocity model.

2 METHODS

In this section, we first briefly review linearized waveform inversion and then discuss dynamic warping, the method we use to estimate traveltime shifts, before presenting our method for amplitude-only inversion.

2.1 Linearized waveform inversion

Wave propagation in the subsurface is described approximately by the constant-density acoustic wave equation,

$$\sigma_0 \frac{\partial^2 u_0}{\partial t^2} - \Delta u_0 = f, \quad (1)$$

where u_0 is the wavefield, σ_0 is the squared background slowness, and f is the source function. Perturbing σ_0 by a scattering potential m and linearizing about m yields

$$\sigma_0 \frac{\partial^2 u}{\partial t^2} - \Delta u = -m \frac{\partial^2 u_0}{\partial t^2}, \quad (2)$$

where u is the scattered or perturbation wavefield. Often m is referred to as the reflectivity model or simply the reflectivity.

Let \mathbf{u}_s denote the discretized solution of equation 2 for a source function at position s . The wavefield \mathbf{u}_s is linear in the reflectivity \mathbf{m} :

$$\mathbf{u}_s = \mathbf{L}_s \mathbf{m}, \quad (3)$$

where \mathbf{L}_s is a linear prediction operator describing the evolution of the scattered wavefield in equation 2. The predicted data $\mathbf{p}_{s,r}$ are a subset of the wavefield \mathbf{u}_s :

$$\mathbf{p}_{s,r} = \mathbf{S}_r \mathbf{u}_s, \quad (4)$$

where \mathbf{S}_r is a sampling operator that extracts the wavefield at receiver position r .

To solve equation 4 for the reflectivity model \mathbf{m} , we minimize, in a least-squares sense, the difference between predicted data $\mathbf{p}_{s,r}$ and observed data $\mathbf{d}_{s,r}$:

$$\min_{\mathbf{m}} J(\mathbf{m}) = \sum_{s,r} E_{s,r}(\mathbf{u}_s(\mathbf{m})), \quad (5)$$

where

$$E_{s,r}(\mathbf{u}_s) = \frac{1}{2} \|\mathbf{S}_r \mathbf{u}_s - \mathbf{d}_{s,r}\|^2. \quad (6)$$

To minimize equation 5, we can pursue the negative of the gradient direction

$$\frac{\partial J}{\partial \mathbf{m}} = \sum_{s,r} \mathbf{L}_s^T \left(\frac{\partial E_{s,r}}{\partial \mathbf{u}_s} \right), \quad (7)$$

where

$$\frac{\partial E_{s,r}}{\partial \mathbf{u}_s} = \mathbf{S}_r^T (\mathbf{S}_r \mathbf{u}_s - \mathbf{d}_{s,r}) \quad (8)$$

is the data residual. The adjoint of the prediction operator \mathbf{L}_s is a migration operator (Claerbout, 1992), and so we obtain the well-known result (Lailly, 1983; Tarantola, 1984) that the gradient of the least-squares misfit function can be computed by a migration of the residuals.

2.2 Dynamic warping

Before we can consider an amplitude misfit function, we require a method for estimating time-varying traveltime shifts between predicted and observed data. For this purpose, we use dynamic warping (Hale, 2013). Compared to more conventional methods for estimating traveltime shifts based on windowed crosscorrelations, dynamic warping is more accurate, especially when traveltime shifts vary rapidly as a function of time (Hale, 2013).

Dynamic time warping (Sakoe and Chiba, 1978) is a method for computing integer time shifts $\boldsymbol{\tau} = (\tau_1, \tau_2, \dots, \tau_n)$ between two sequences $\mathbf{p} = (p_1, p_2, \dots, p_n)$ and $\mathbf{d} = (d_1, d_2, \dots, d_n)$ such that

$$A = \frac{1}{2} \sum_i (p_i - d_{i+\tau_i})^2 \quad (9)$$

is minimized with respect to $\boldsymbol{\tau}$ subject to the constraint

$$|\tau_i - \tau_{i-1}| \leq 1/c, \quad (10)$$

where c is a positive integer. An attractive feature of dynamic time warping is that the algorithm is guaranteed to find the traveltimes shifts $\boldsymbol{\tau}$ that minimize equation 9 subject to constraint 10, and these shifts are such that $\partial A/\partial \boldsymbol{\tau} = \mathbf{0}$ when the constraint is inactive.

Although we could use dynamic time warping to independently estimate traveltimes shifts between all pairs of predicted and observed traces, in practice we find that using dynamic image warping (Hale, 2013) to estimate traveltimes shifts between predicted and observed common shot gathers yields more accurate shifts, especially when predicted and observed data are not simply shifted versions of each other (as is often the case even with synthetic data, and certainly always is the case with recorded field data). Dynamic image warping (Hale, 2013) approximately solves the extension to higher dimensions of the constrained optimization problem specified by equations 9 and 10, and in doing so, imposes constraints both in time (equation 10) as well as in distance or offset on the estimated traveltimes shifts.

2.3 Inversion of amplitude errors

To formulate an inversion of amplitude errors, we modify the observed data to include a time-shift operator:

$$\mathbf{b}_{s,r} = \mathbf{T}_{s,r} \mathbf{d}_{s,r}, \quad (11)$$

where $\mathbf{T}_{s,r}$ is a linear operator, e.g., a sinc interpolation operator, that shifts the observed data $\mathbf{d}_{s,r}$ by the traveltimes shifts $\boldsymbol{\tau}_{s,r}$ estimated using dynamic warping. Note that $\mathbf{T}_{s,r}$ depends implicitly on the model \mathbf{m} , because the traveltimes shifts $\boldsymbol{\tau}_{s,r}$ are computed using the predicted data $\mathbf{p}_{s,r}$, which depend on the model.

The shifted observed data $\mathbf{b}_{s,r}$ can be viewed as a secondary dataset obtained by processing the observed data. Processing of the observed data prior to migration is standard practice, even for conventional migration. The purpose of this processing is essentially to remove from the observed data any components that are due to an inconsistent model of wave propagation in the true subsurface. For example, in order to use acoustic forward modeling to migrate elastic data, one would need to remove shear waves from observed data prior to migration. Just as an acoustic wave equation cannot explain shear waves in observed data, the linearized wave equation (equation 2) with an incorrect background model cannot explain the traveltimes of observed data. Migration using an incorrect background model is equivalent to migration using forward modeling that is inconsistent with the observed data, and so to properly migrate these data, we must first remove those components that cannot be explained by our forward modeling. Those components are the traveltimes.

Thus, we seek to minimize the difference between

predicted data $\mathbf{p}_{s,r}$ and time-shifted observed data $\mathbf{b}_{s,r}$:

$$\min_{\mathbf{m}} J_A(\mathbf{m}) = \sum_{s,r} A_{s,r}(\mathbf{u}_s(\mathbf{m}), \boldsymbol{\tau}_{s,r}(\mathbf{m})), \quad (12)$$

where

$$A_{s,r} = \frac{1}{2} \|\mathbf{S}_r \mathbf{u}_s - \mathbf{T}_{s,r} \mathbf{d}_{s,r}\|^2. \quad (13)$$

Note that if the estimated traveltimes shifts $\boldsymbol{\tau}_{s,r}$ are accurate, then equation 12 measures only amplitude errors between predicted and observed data. If the traveltimes shifts are zero, then equation 12 reduces to equation 5.

To minimize the misfit function in equation 12, we require its gradient with respect to model parameters:

$$\frac{\partial J_A}{\partial \mathbf{m}} = \sum_{s,r} \mathbf{L}_s^\top \left(\frac{\partial A_{s,r}}{\partial \mathbf{u}_s} \right), \quad (14)$$

where

$$\frac{\partial A_{s,r}}{\partial \mathbf{u}_s} = \mathbf{S}_r^\top (\mathbf{S}_r \mathbf{u}_s - \mathbf{T}_{s,r} \mathbf{d}_{s,r}). \quad (15)$$

Although $A_{s,r}$ depends on the estimated traveltimes shifts $\boldsymbol{\tau}_{s,r}$, we need not consider this dependence when computing the residual in equation 15 because dynamic warping minimizes equation 13 (or equation 9) subject to constraint 10, so that $\partial A_{s,r}/\partial \boldsymbol{\tau}_{s,r}$ is mostly zero. We refer to equation 15 as the amplitude residual and equation 12 as the amplitude misfit function, as they measure only amplitude errors between predicted and observed data.

3 RESULTS

We compare conventional least-squares migration (LSM) with the proposed method of least-squares migration of amplitude errors (LSMA) on a 2D synthetic dataset, and on a 2D field dataset.

For least-squares migration, the data are linear in the reflectivity, and thus LSM images can be computed by minimizing equation 5 with (linear) conjugate gradient iterations. To compute LSMA images by solving equation 12, however, is a nonlinear problem because the reflectivity \mathbf{m} depends on the traveltimes shifts $\boldsymbol{\tau}_{s,r}$, but the traveltimes shifts also depend on the reflectivity. We can compute LSMA images either by minimizing equation 12 using a gradient-based descent method (e.g., steepest descent or nonlinear conjugate gradient), or alternatively, by first solving equation 12 with fixed traveltimes shifts $\boldsymbol{\tau}_{s,r}$, then recomputing the traveltimes shifts and solving equation 12 with the new shifts, repeating until convergence.

Note that when the traveltimes shifts $\boldsymbol{\tau}_{s,r}$ are zero, equation 12 is equivalent to equation 5. This is the case for the first nonlinear iteration or the first solution of equation 12 with fixed $\boldsymbol{\tau}_{s,r}$, in which the reflectivity is zero and hence the traveltimes shifts are zero. After the first nonlinear iteration or the first solution of equa-

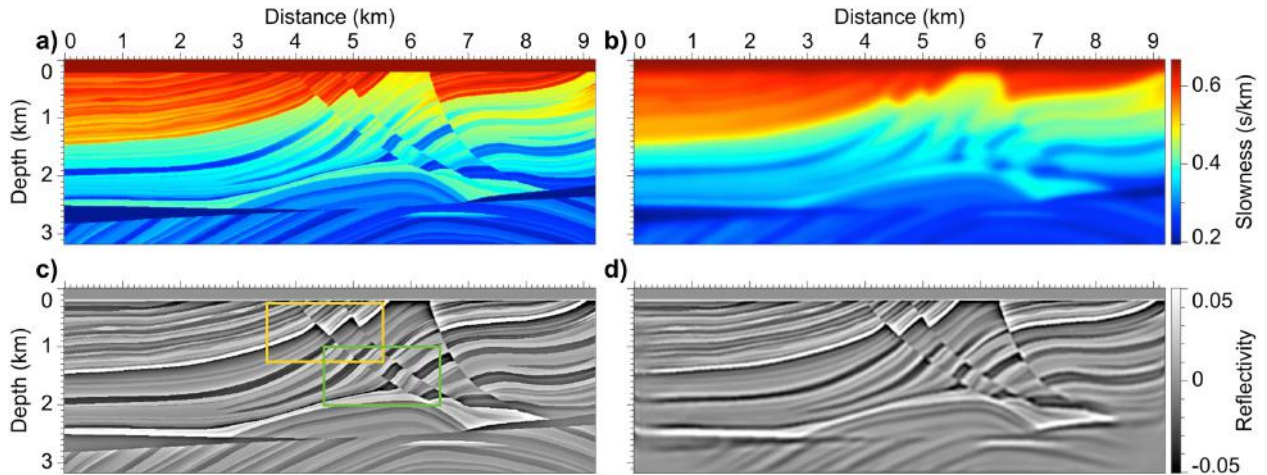


Figure 3. The (a) true slowness model, (b) true background slowness model, (c) true reflectivity computed as the difference between the true slowness squared and the true background slowness squared, and (d) LSM image.

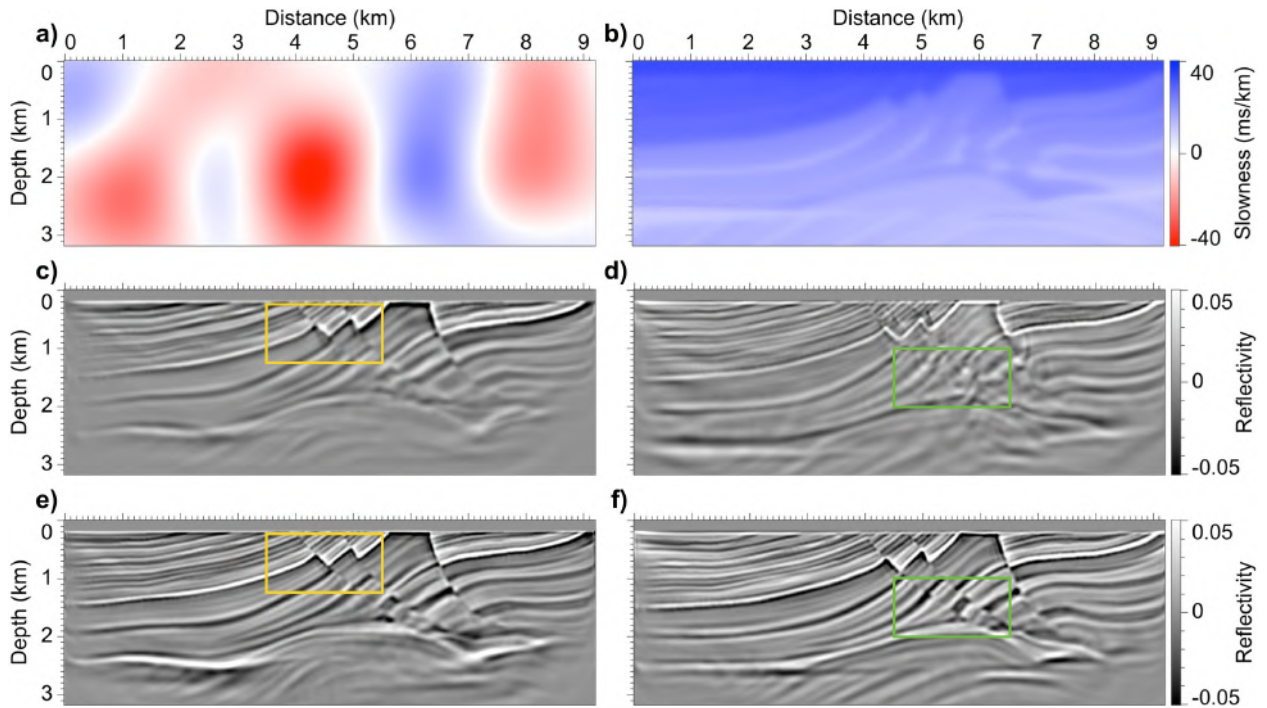


Figure 4. The (a,b) difference between the true background slowness shown in Figure 3b and the background slowness used for migration; (c) LSM image computed for the background slowness with error shown in (a); (d) LSM image computed for the background slowness with error shown in (b); (e) LSMA image computed for the background slowness with error shown in (a); and (f) LSMA image computed for the background slowness with error shown in (b).

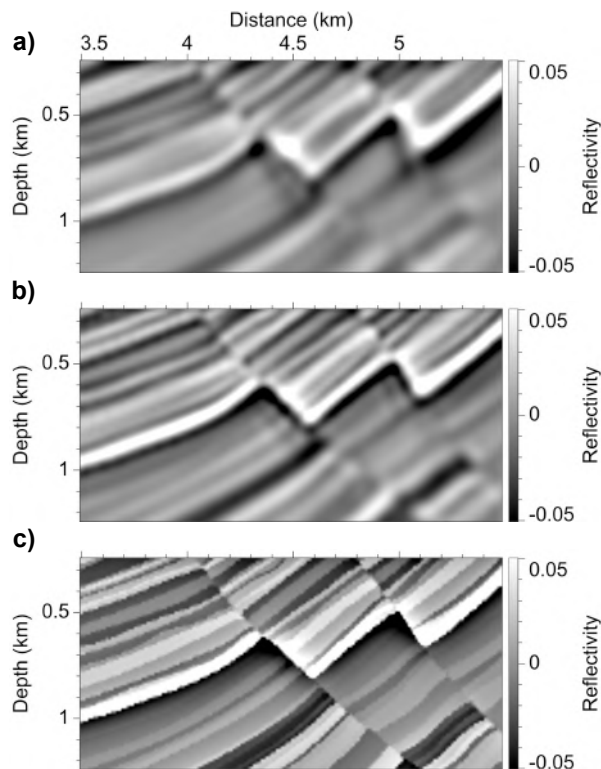


Figure 5. Zoomed views of the areas enclosed by yellow boxes in the (a) LSM image in Figure 4c, (b) LSMA image in Figure 4e, and (c) true reflectivity in Figure 3c.

tion 12, we obtain a nonzero reflectivity image from which to predict data and to estimate possibly nonzero traveltimes shifts.

3.1 Synthetic data example

The background slowness used for modeling and migration is shown in Figure 3b, and is computed by smoothing a modified Marmousi model (Lailly and Versteeg, 1990) shown in Figure 3a along both the depth and distance axes using a two-sided exponential filter with width 100 m. The true reflectivity shown in Figure 3c is then computed as the difference between the true slowness (Figure 3a) squared and the true background slowness (Figure 3b) squared. Using the true background slowness and true reflectivity, we simulate observed data by solving equations 1 and 2 for a Ricker source function with peak frequency 10 Hz. To facilitate comparison of LSM and LSMA, all migration images for these synthetic data are computed using 20 nonlinear conjugate gradient iterations. Hence, as the cost of dynamic warping is small compared to the cost of modeling and migration, the LSM and LSMA images computed for these synthetic data come at comparable costs.

The first example shown in Figure 3 demonstrates conventional LSM using the true background slowness

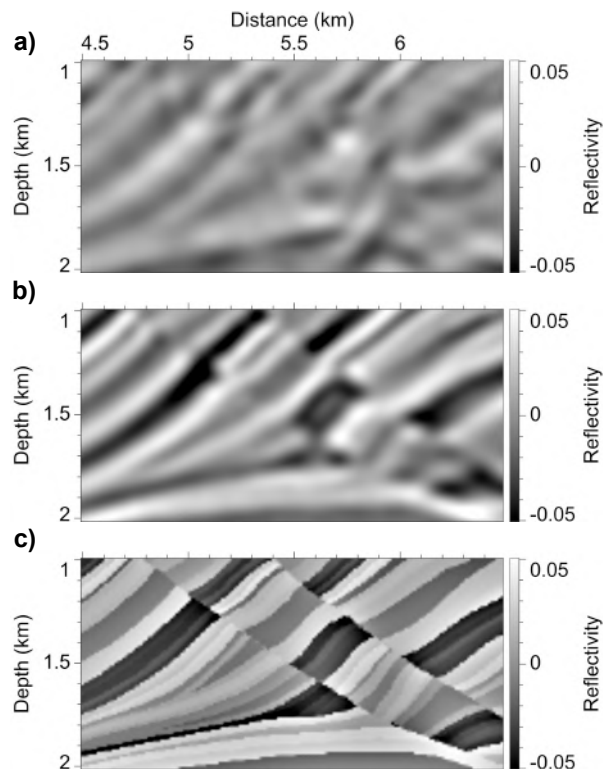


Figure 6. Zoomed views of the areas enclosed by green boxes in the (a) LSM image in Figure 4d, (b) LSMA image in Figure 4f, and (c) true reflectivity in Figure 3c.

for migration. The reflectivity image shown in Figure 3d is obtained after 20 nonlinear conjugate gradient iterations (Nocedal and Wright, 2000) of LSM using the true background slowness with 153 shots and 767 receivers evenly spaced along the surface. As expected, this computed reflectivity matches well the true reflectivity shown in Figure 3c because the background slowness model used for migration was exactly the true background slowness. In practice, we expect the background slowness model used to migrate the data to differ from the true background slowness model.

Figure 4 illustrates the effects of erroneous background slowness models on the reflectivity images obtained using LSM and LSMA. Figures 4a and 4b show the differences between the true background slowness model (Figure 3b) and the background slowness models that we use for migration. The slowness error shown in Figure 4a was computed by smoothing a random slowness model, while the error shown in Figure 4b resulted from scaling the true background slowness by 95%.

Figures 4c and 4d show the reflectivity images computed using 20 iterations of LSM with the erroneous background slowness models with errors shown in Figures 4a and 4b, respectively. Compared to the reflectivity image (Figure 3d) computed using the true background slowness, the image in Figure 4c is degraded, and

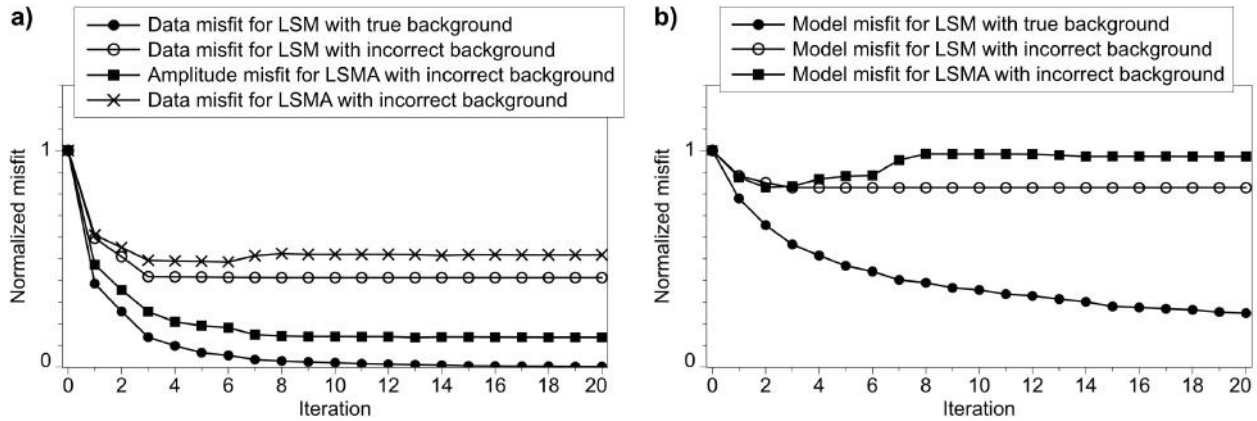


Figure 7. Normalized (a) data and amplitude misfit and (b) model misfit for LSM and LSMA. Here, *true background* refers to the true background slowness shown in Figure 3b, while *incorrect background* refers to the background slowness with error shown in Figure 4a.

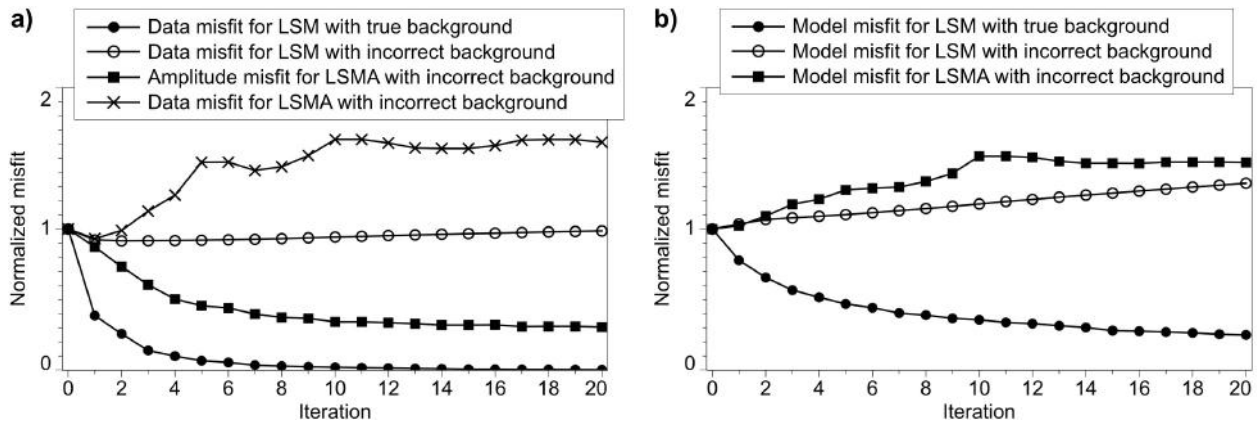


Figure 8. Normalized (a) data and amplitude misfit and (b) model misfit for LSM and LSMA. Here, *true background* refers to the true background slowness shown in Figure 3b, while *incorrect background* refers to the background slowness with error shown in Figure 4b.

shows uneven illumination and defocused reflectors, especially at greater depths where traveltimes errors resulting from the erroneous background slowness are more severe. This degradation is also seen in the reflectivity image shown in Figure 4d. The quality of this image is worse than the image shown in Figure 4c because the slowness errors (Figure 4b) all have the same sign, and so traveltimes errors in the predicted data accumulate more quickly than traveltimes errors for data predicted with the slowness model with error shown in Figure 4a.

Figures 4e and 4f show the reflectivity images computed with 20 iterations of LSMA. Compared to the conventional LSM images (Figures 4c and 4d), the LSMA images show improved illumination of deeper portions of the model, and better focused and more continuous reflectors throughout. For example, Figures 5a, 5b, and 5c show zoomed views of the areas enclosed by yellow boxes in Figures 4c, 4e, and 3c, respectively. Compared to the LSM image shown in Figure 5a, reflectors

in the LSMA image shown in Figure 5b are more focused and better match the true reflectivity shown in Figure 5c. Similarly, zoomed views shown in Figures 6a, 6b, and 6c of the areas enclosed by green boxes in Figures 4d, 4f, and 3c, respectively, demonstrate that even for a large and biased slowness error (Figure 4b), minimizing the amplitude misfit function yields an interpretable reflectivity image with features that match those apparent in the true reflectivity.

Note, however, that the positions of features in LSMA images (Figures 4e and 4f) are shifted compared to their positions in the true reflectivity (Figure 3c). For example, compare the position of the reflector located at distance 3.5 km and depth 1 km in Figure 5b, or the reflector located at distance 4.5 km and depth 1 km in Figure 6b, to their positions in the true reflectivity. This mispositioning is expected, however, since LSMA images are computed using erroneous background slowness models.

The presence of remaining traveltimes shifts between predicted and observed data, as well as spatial shifts between image features in computed LSMA images and those in the true reflectivity, is confirmed by the misfit functions shown in Figures 7 and 8. Figures 7a and 8a show normalized data and amplitude misfit functions, while Figures 7b and 8b show normalized model misfit functions (the L^2 -norm of the difference between the computed reflectivity and the true reflectivity) for LSM and LSMA images computed using either the true background slowness model shown in Figure 3b or the erroneous background slowness model with error shown in Figure 4a or Figure 4b. In Figures 7a and 8a, note that the data misfit is not used in LSMA, but more importantly, notice that the data misfit increases in iteration 7 in Figure 7a and in iteration 2 in Figure 8a. This indicates that the better-focused LSMA images shown in Figures 4e and 4f *cannot be obtained with conventional LSM*, which minimizes the data misfit.

The model misfits shown in Figures 7b and 8b indicate that, for the erroneous background slowness models shown in Figures 4a and 4b, the LSM images (Figures 4c and 4d) more closely match the true reflectivity (Figure 3c) than do the LSMA images (Figures 4e and 4f). Indeed, a zero-reflectivity image is closer to the true reflectivity than the LSMA image shown in Figure 4f. However, the large model misfits for LSMA images simply reflect the fact that features in these images are shifted relative to the corresponding features in the true reflectivity. Although image features in LSMA images are shifted, it is clear that the amplitudes (but not the positions) of these features better match those of the true reflectivity.

3.2 Field data example

Next we test our method for amplitude-only migration on a subset of a field dataset provided by Eni E&P. The entire 2D dataset contains 3661 shots with a shot spacing of 12.5 m, and was recorded using a streamer with 99 receivers with a receiver spacing of 12.5 m and maximum offset of 1.225 km. The subset of the data that we migrate consists of 431 shots with shot spacing of 25 m. The data have been regularized, and multiples have been attenuated. We estimate a zero-phase wavelet from the amplitude spectrum computed from a subset of the recorded data (Claerbout, 1992), and we apply a bandpass filter to both the estimated wavelet and the recorded data to remove frequency content below 10 Hz and above 40 Hz prior to migration.

We compare LSM and LSMA for two slowness models. The first slowness model, shown in Figure 9a, is laterally invariant (except near the sea floor), while the second, shown in Figure 9b, is an optimized slowness model that was provided with the recorded data. The LSM and LSMA images computed for the laterally invariant slowness model (Figure 9a) are shown in Fig-

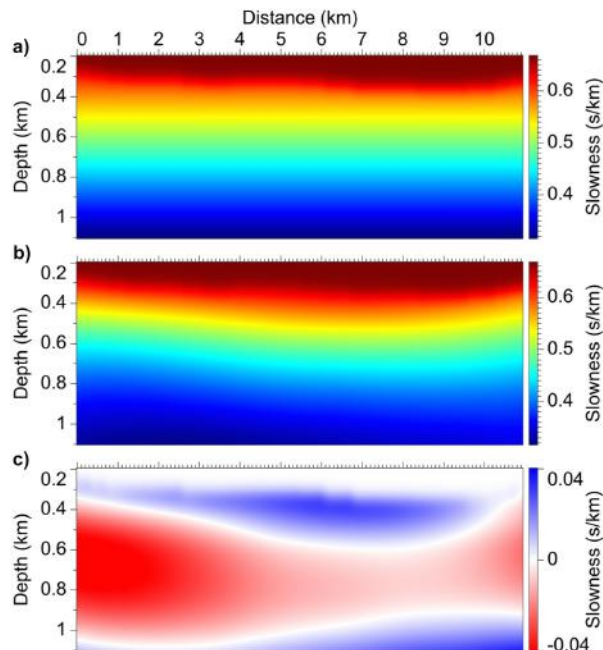


Figure 9. The (a) laterally invariant and (b) optimized slowness models used for migration, and the (c) difference between (b) and (a).

ures 10a and 10b, respectively. Comparing these images, we observe that reflectors in the LSMA image are more continuous and better focused than corresponding reflectors in the LSM image. Moreover, image features in the LSMA image (Figure 10b) are similar to features seen in the LSM image (Figure 10c) computed for the optimized slowness model (Figure 9b), despite the use of a much simpler slowness model for LSMA. Differences between the migration images shown in Figures 10a and 10b are most apparent in the areas enclosed by yellow boxes, in which the slowness differences (Figure 9c) between the models used for migration are relatively large. Zoomed views of the areas enclosed by yellow boxes in Figures 10a, 10b, and 10c are shown in Figures 1a, 1b, and 1c, respectively. Elsewhere, where slowness errors are smaller, differences between the migration images are less significant, as one would expect.

It is worth noting that, for this example, it was necessary to use 3D dynamic warping in LSMA. For 3D warping, rather than independently warp predicted to observed shot gathers as was done for the synthetic examples shown in Figure 4, we instead warped simultaneously all predicted shot gathers to all observed shot gathers, at each iteration of LSMA. A 3D warping enables us to constrain changes in estimated traveltimes with shot location, which results in more accurate shifts. For synthetic tests in which the same forward modeling code is used to simulate both predicted and observed data, this additional constraint is per-

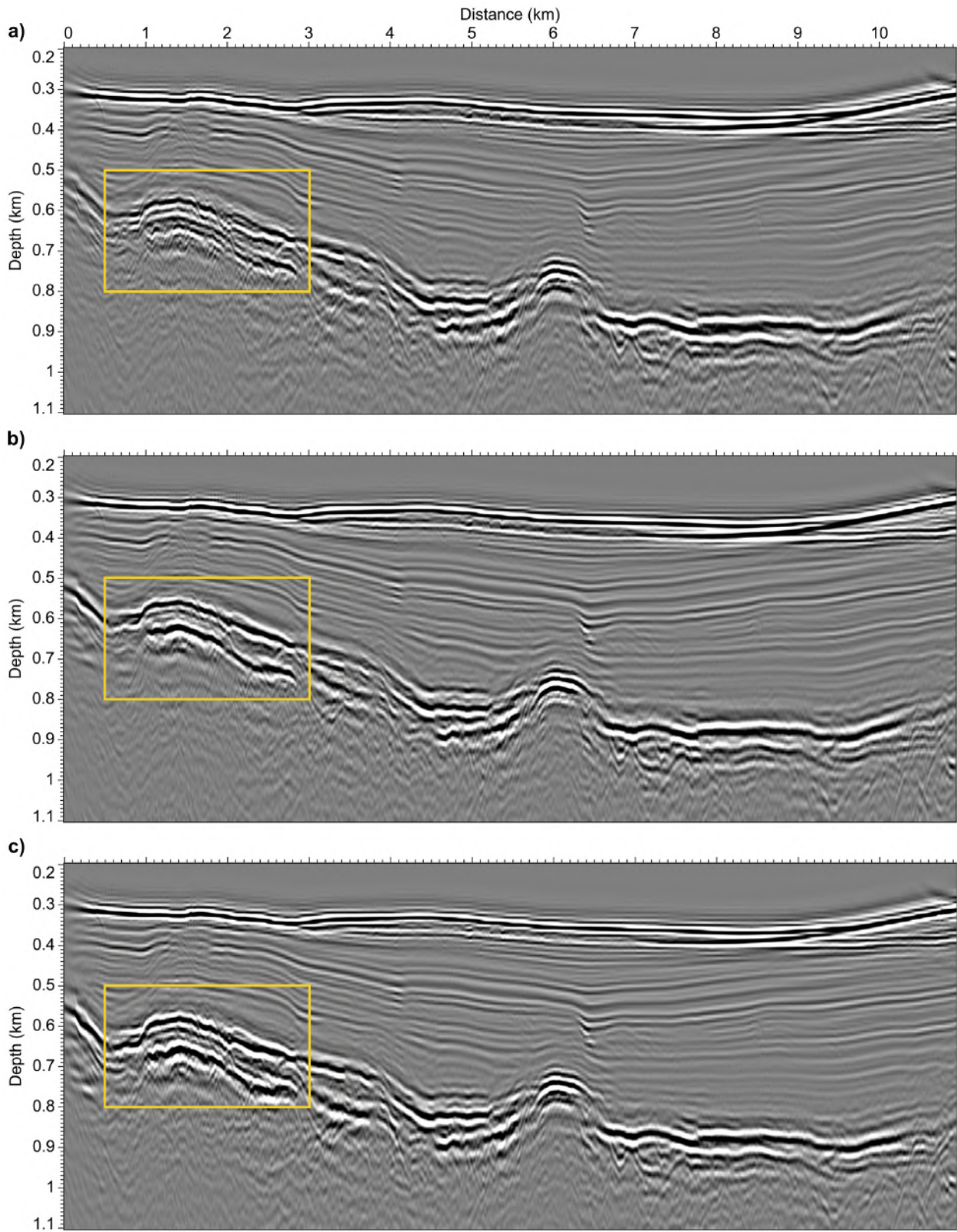


Figure 10. The (a) LSM image and (b) LSMA image computed for the laterally invariant slowness model shown in Figure 9a, and the (c) LSM image computed for the optimized slowness model shown in Figure 9b.

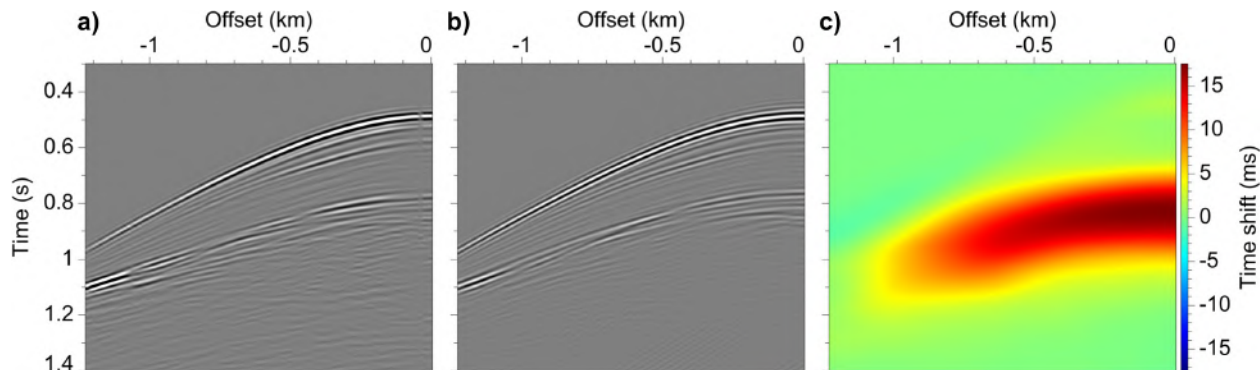


Figure 11. For the shot located at distance 1.85 km, the (a) observed data, (b) predicted data computed using the laterally invariant slowness model shown in Figure 9a and the LSMA image shown in Figure 10b, and (c) traveltime shifts between (a) and (b).

haps unnecessary. For field data, however, an additional constraint on the traveltime shifts can significantly improve the accuracy of estimated shifts, especially in cases where the data quality is low.

Because we compute LSMA images by minimizing the difference between predicted and shifted observed data (equation 12), the predicted data in general will not have the same traveltimes as the original observed data. An example of these traveltime differences for data corresponding to the shot located at distance 1.85 km is shown in Figure 11. Figure 11a shows the observed data, Figure 11b shows the predicted data computed using the laterally invariant slowness model (Figure 9a) and the LSMA image (Figure 10b), and Figure 11c shows the traveltime shifts between the data shown in Figures 11a and 11b. The maximum frequency content of the data is 40 Hz, which corresponds to a period of 25 ms. Thus we observe from Figure 11c that the remaining traveltime shifts between predicted and observed data exceed one half period. This confirms that LSMA yields an image that explains the dynamics, but not the kinematics, of the observed data.

4 CONCLUSION

We have presented a method for least-squares migration that minimizes an amplitude misfit function defined with differences between predicted data and shifted observed data, with traveltime shifts between predicted and observed data estimated using dynamic warping. The use of this amplitude misfit function results in a more coherent and better focused migration image when the background slowness model used for migration contains errors. These LSMA images contain image features with amplitudes that match those of the true reflectivity, but with positions that are shifted relative to the positions of corresponding features in the true reflectivity. LSMA images thus are better suited for interpretation of geologic structures, but in order to correctly position

interpreted structures, we would need to first correctly position LSMA image features. One way to correct for the mispositioning of image features is to first align features with measurements of subsurface properties obtained from well logs, and then interpolate alignment shifts between well-log locations to generate shifts for an entire image.

The improvement in LSMA images compared to conventional LSM images depends on the nature of the background slowness error, and also on the acquisition geometry. A comparison between the images shown in Figure 4e and 4f suggests that LSMA provides a greater improvement in image quality and reflector focusing for small, systematic errors in background slowness (e.g., Figure 4b), perhaps because in such situations, traveltime shifts can explain well the differences between predicted and observed data. When the background slowness error is more complex or is too large, predicted and observed data might be inconsistent, i.e., events in one dataset do not have corresponding events in the other, making it difficult to estimate accurate shifts; or, predicted and observed data might differ by significant horizontal spatial shifts in addition to vertical traveltime shifts, in which case estimating only traveltime shifts for use in LSMA might be inadequate. While dynamic warping can also be used to estimate horizontal shifts, only vertical traveltime shifts were used in the examples shown above.

The improvement in LSMA images also depends on acquisition geometry. Traveltime differences between observed and predicted data in LSM arise from errors in the background slowness model used for migration, but more specifically, they arise from inconsistencies between different images of the same subsurface geologic structures, e.g., images computed for neighboring individual shots. Thus, we expect LSMA to provide greater improvement over conventional LSM when the recorded data provide redundant information about subsurface geologic structures. Conversely, we expect LSMA and

LSM images to be more similar when data provide independent information, for example, when shots are sparsely located or shot spacing is large, or when the maximum source-receiver offset or the offset-to-depth ratio is small.

Although LSMA images can provide an improved estimate of the amplitudes of the true reflectivity, ultimately we seek a complete model of the subsurface, which includes not only an accurate reflectivity model but also an accurate background slowness model. The proposed method could potentially be extended and used to aid an inversion for the background slowness. A simple approach might be to hold the reflectivity model constant following LSMA, and then invert the remaining traveltime shifts between predicted and observed data in order to update the background slowness.

5 ACKNOWLEDGEMENT

This work was supported by the sponsors of the Consortium Project on Seismic Inverse Methods for Complex Structures at the Colorado School of Mines. Thanks to Clément Fleury for helpful discussions and for sharing his insights on this problem. Thanks also to Eni E&P for providing the field data.

REFERENCES

- Baysal, E., D. Kosloff, and J. Sherwood, 1983, Reverse time migration: *Geophysics*, **48**, 1514–1524.
- Bednar, J. B., C. Shin, and S. Pyun, 2007, Comparison of waveform inversion, part 2: phase approach: *Geophys. Prospect.*, **55**, 455–465.
- Chavent, G., and R. Plessix, 1999, An optimal true-amplitude least-squares prestack depth-migration operator: *Geophysics*, **64**, 508–515.
- Choi, Y., and T. Alkhalifah, 2011, Frequency-domain waveform inversion using the unwrapped phase: 81st Annual International Meeting, SEG, Expanded Abstracts.
- Claerbout, J. F., 1992, *Earth soundings analysis: Processing versus inversion*: Blackwell Scientific Publications.
- Cohen, J. K., and N. Bleistein, 1979, Velocity inversion procedure for acoustic waves: *Geophysics*, **44**, 1077–1087.
- Dai, W., 2012, *Multisource least-squares reverse time migration*: PhD thesis, King Abdullah University of Science and Technology.
- Gray, S., 1997, True amplitude migration: a comparison of three approaches: *Geophysics*, **62**, 929–936.
- Guitton, A., 2004, Amplitude and kinematic corrections of migrated images for nonunitary imaging operators: *Geophysics*, **69**, 1017–1024.
- Hale, D., 2013, Dynamic warping of seismic images: *Geophysics*, **78**, S105–S115.
- Hicks, G., and R. Pratt, 2001, Reflection waveform inversion using local descent methods: Estimating attenuation and velocity over a gassand deposit: *Geophysics*, **66**, 598–612.
- Kamei, R., A. J. Brenders, and R. G. Pratt, 2011, A discussion on the advantages of phase-only waveform inversion in the Laplace-Fourier domain: Validation with marine and land seismic data: 81st Annual International Meeting, SEG, Expanded Abstracts.
- Kühl, H., and M. D. Sacchi, 2003, Least-squares wave-equation migration for AVP/AVA inversion: *Geophysics*, **68**, 262–273.
- Lailly, P., 1983, The seismic inverse problem as a sequence of before stack migration: Conference on Inverse Scattering: Theory and Applications, SIAM, 206–220.
- Lailly, P., and R. Versteeg, 1990, The Marmousi workshop – Introduction: Proceedings of the 52nd EAGE Workshop – Practical Aspects of Seismic Data Inversion.
- Levin, S., 1984, Principle of reverse-time migration: *Geophysics*, **49**, 581–583.
- Loewenthal, D., and I. Mufti, 1983, Reversed time migration in spatial frequency domain: *Geophysics*, **48**, 627–635.
- Ma, Y., 2012, *Waveform-based velocity estimation from reflection seismic data*: PhD thesis, Colorado School of Mines.
- McMechan, G. A., 1983, Migration by extrapolation of time-dependent boundary values: *Geophys. Prospect.*, **31**, 413–420.
- Nemeth, T., C. Wu, and G. T. Schuster, 1999, Least-squares migration of incomplete reflection data: *Geophysics*, **64**, 208–221.
- Nocedal, J., and S. J. Wright, 2000, *Numerical optimization*: Springer Science+Business Media, LLC.
- Østmo, S., and R.-E. Plessix, 2002, Finite-difference iterative migration by linearized waveform inversion in the frequency domain: 72nd Annual International Meeting, SEG, Expanded Abstracts.
- Plessix, R.-E., and W. A. Mulder, 2004, Frequency-domain finite-difference amplitude-preserving migration: *Geophys. J. Int.*, **157**, 975–987.
- Pratt, R. G., C. Shin, and G. Hicks, 1998, Gauss-newton and full newton methods in frequency-space seismic waveform inversion: *Geophys. J. Int.*, **113**, 341–462.
- Rickett, J. E., 2003, Illumination-based normalization for wave-equation depth migration: *Geophysics*, **68**, 1371–1379.
- Sakoe, H., and S. Chiba, 1978, Dynamic programming algorithm optimization for spoken word recognition: *IEEE Transactions on Acoustics, Speech, and Signal Processing*, **26**, 43–49.
- Shin, C., S. Jang, and D. J. Min, 2001, Improved amplitude preservation for prestack depth migration by inverse scattering theory: *Geophys. Prospect.*, **49**, 592–

606.

- Shin, C., and D. J. Min, 2006, Waveform inversion using a logarithmic wavefield: *Geophysics*, **71**, R31–R42.
- Snieder, R., M. Xie, A. Pica, and A. Tarantola, 1989, Retrieving both the impedance contrast and background velocity: A global strategy for the seismic reflection problem: *Geophysics*, **54**, 991–1000.
- Symes, W. W., 2008, Approximate linearized inversion by optimal scaling of prestack depth migration: *Geophysics*, **73**, R23–R35.
- , 2009, The seismic reflection inverse problem: *Inverse Problems*, **25**, 1–39.
- Tarantola, A., 1984, Inversion of seismic reflection data in the acoustic approximation: *Geophysics*, **49**, 1259–1266.
- Valenciano, A., 2008, Imaging by wave-equation inversion: PhD thesis, Stanford University.
- Whitmore, N. D., 1983, Iterative depth migration by backward time propagation: 53rd Annual International Meeting, SEG, Expanded Abstracts, 382–385.
- Xu, S., 2012, Full waveform inversion for reflected seismic data: 74th EAGE Conference and Exhibition, Extended Abstracts.